AD-A094 325 UNITED TECHNOLOGIES RESEARCH CENTER EAST HARTFORD CONN F/G 11/6
A STUDY OF THE DEPENDENCE OF MICROSEGREGATION ON CRITICAL SOLID--ETC(U)
DEC 80 L E GREENWALD, H L FRASER, M J KAUFMAN N00014-79-C-0649
UNCLASSIFIED UTRC/R80-914763-3 NL

1 OF 1
AD A094325

END
DATE FILMED
2-81
DTIC

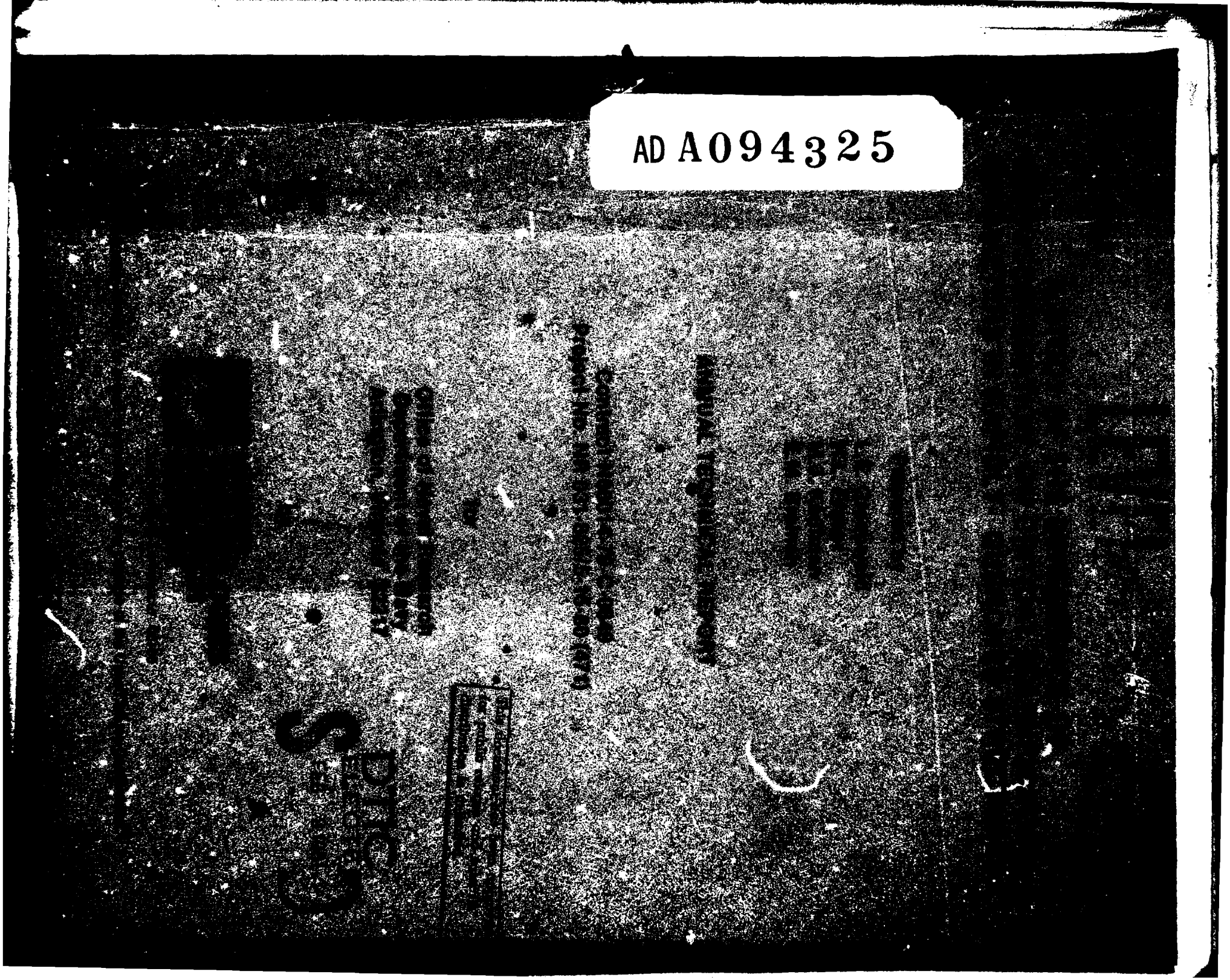

UNCLASSIFIED
SECURITY CLASSIFICATION OF THIS PAGE (When Data Entered)

REPORT DOCUMENTATION PAGE

READ INSTRUCTIONS BEFORE COMPLETING FORM

1. REPORT NUMBER: UTRC/R80-914763-3	2. GOVT ACCESSION NO.: AD94325
3. RECIPIENT'S CATALOG NUMBER:	
4. TITLE (and Subtitle): A STUDY OF THE DEPENDENCE OF MICROSEGREGATION ON CRITICAL SOLIDIFICATION PARAMETERS IN RAPIDLY-QUENCHED STRUCTURES	5. TYPE OF REPORT & PERIOD COVERED: Annual Technical Report, 1 Aug 1979 — 30 Sept 1980
	6. PERFORMING ORG. REPORT NUMBER:
7. AUTHOR(s): L. E. Greenwald, H. L. Fraser, M. J. Kaufman, E. M. Breinan	8. CONTRACT OR GRANT NUMBER(s): N00014-79-C-0649
9. PERFORMING ORGANIZATION NAME AND ADDRESS: United Technologies Research Center, East Hartford, CT 06108	10. PROGRAM ELEMENT, PROJECT, TASK AREA & WORK UNIT NUMBERS: 471
11. CONTROLLING OFFICE NAME AND ADDRESS: Office of Naval Research, Department of the Navy, Arlington, VA 22217	12. REPORT DATE: December 1980
	13. NUMBER OF PAGES: 41
14. MONITORING AGENCY NAME & ADDRESS (if different from Controlling Office)	15. SECURITY CLASS. (of this report): Unclassified
	15a. DECLASSIFICATION/DOWNGRADING SCHEDULE:

16. DISTRIBUTION STATEMENT (of this Report)

Reproduction in whole or in part is permitted for any purpose of the United States Government

17. DISTRIBUTION STATEMENT (of the abstract entered in Block 20, if different from Report)

18. SUPPLEMENTARY NOTES

19. KEY WORDS (Continue on reverse side if necessary and identify by block number)

Microsegregation	Heat Transfer Calculations
Solidification Cracking	Deep Penetration Laser Melting
Critical Solidification Parameters	Shallow Penetration Laser Melting
Rapidly Quenched Structures	Cooling Rates

20. ABSTRACT (Continue on reverse side if necessary and identify by block number)

The aims of the present program were to determine both experimentally and analytically the cooling rates experienced by material during laser melting in the deep penetration and shallow penetration melting modes, to determine the microstructures and degrees of microsegregation associated with these cooling rates, to correlate the structure and segregation with weld cracking behavior, and to eventually determine the mechanism involved in weld cracking. A literature survey was performed and two new mathematical models were

DD FORM 1 JAN 73 1473 EDITION OF 1 NOV 65 IS OBSOLETE

UNCLASSIFIED
SECURITY CLASSIFICATION OF THIS PAGE (When Data Entered)

#19. Cont'd

Literature Survey/Heat Transfer
Model Development/Heat Transfer
One Dimensional Model
Two Dimensional Model
Validation Experiments

#20. Cont'd

developed, a two dimensional model for deep penetration welding and a one dimensional model for shallow penetration surface melting. The results of both model calculations were eventually verified by experimental tests and comparisons of results, with excellent agreement being obtained for the deep penetration model and adequate agreement being obtained for the shallow penetration model.

In addition a series of three special Ni-Al-Mo alloys was weld-crack tested to determine effects of microstructure on cracking behavior. Since general observations of composition and solidification conditions did not permit explanation of cracking behavior, microstructural observations were made on chill cast and brine-quenched microstructures. The predominant microstructural factor which seems to affect cracking behavior at this time in the program appears to be the morphology of the grain boundary. Although it presently appears that significant γ' at the grain boundaries lends added ductility to the material, especially when it is in the form of continuous layers, further research in this area seems warranted, and is under way.

UNITED TECHNOLOGIES RESEARCH CENTER

UNITED TECHNOLOGIES

East Hartford, Connecticut 06108

R80-914763-3

A Study of the Dependence of Microsegregation on Critical Solidification Parameters in Rapidly-Quenched Structures

ANNUAL TECHNICAL REPORT
N00014-79-C-0649

REPORTED BY L. E. Greenwald

H. L. Fraser

M. J. Kaufman

E. M. Breinan

APPROVED BY E. R. Thompson, Manager
Materials Sciences

DATE _____

NO. OF PAGES _____ **COPY NO.** _____

A Study of the Dependence of Microsegregation on Critical Solidification Parameters in Rapidly-Quenched Structures

TABLE OF CONTENTS

INTRODUCTION

The aims of the present program have been twofold in nature; first, to determine, using both experimental and analytical techniques, the cooling rates experienced by material during laser processing in both the deep penetration and shallow penetration melting modes, and second, to determine the role of microstructure and microsegregation in the mechanism of laser weld cracking. It was also hoped that the heat-flow calculations in the first part of the program might be used to correlate microstructural phenomena with processing parameters in the materials analysis studies. During the first year of the program, it has not been possible to realize this latter correlation, but it is intended to attempt this during the next program year. Consequently, the report is divided into two sections, one dealing with Tasks I and II (Mathematical Analysis and Validation) and one with Materials Analysis. Both sections show good progress made regarding the achievement of the goals of the work statement. As is common with most research programs, the results have pointed to a number of very interesting questions, the study of which should lead to an increased understanding of laser weld cracking.

TASKS I AND II - MATHEMATICAL ANALYSIS AND MODEL VALIDATION

A. Literature Survey

A literature survey of the types of heat transfer models applicable to the laser welding area has been performed. As expected, much work has been done in this area, but shortcomings exist in most of the models. For example, they are either too complicated for use in parametric or sensitivity studies, or they are not sufficiently detailed to provide the required heat transfer parameters at the melt interface such as cooling rate or freezing rate. Many of the models required lengthy numerical integration techniques for solution, a method which is costly and time consuming (and often unreliable) in terms of computer application. Over 50 papers on the heat transfer analysis of laser welding were obtained and studied.

B. Model Development

Two heat transfer models were selected for computer programming, one for the two-dimensional (2-D) deep-welding process and one for the one-dimensional shallow welding process. The following sections describe the mathematical development of the analytical models and the experiments that were conducted to validate them.

1. 2-D Deep Welding Model

The 2-D heat transfer model of the deep-penetration welding process is shown in Fig. 1 and is based on a formulation given in many sources (Refs. 1-3). The laser is assumed to penetrate completely through the material (making a "keyhole") and the heat transfer is considered to be two-dimensional. A steady-state heat transfer condition is assumed to prevail after startup and the laser beam moves with speed V through the material as shown. Since the heat transfer is assumed to be two-dimensional, the input power must be absorbed uniformly with depth. If P (watts) is the amount of power absorbed by the material (which can be measured calorimetrically) then the power is absorbed at a linear rate $q = P/d$ W/cm where d is the depth of the material in cm. The geometry of the temperature field is shown in Fig. 2a as viewed normal to the surface of the material. The figure depicts the isotherm defining the melt interface, i.e., the locus of points where the temperature is equal to the melting temperature, T_{melt}. The temperature field will appear steady with time if viewed by an observer moving with the laser beam and this coordinate system is used when calculating the geometry of the melt region. Variations of temperature with time, t, can be calculated by reference to a fixed coordinate system shown in Fig. 2b.

Assuming that material properties do not vary with temperature, that the material is uniform, homogeneous and at a constant initial temperature, and neglecting latent heat, the temperature field is given by

$$T-T_o = \frac{q}{2\pi k} e^{-\frac{Vr \cos \phi}{2\alpha}} K_o\left(\frac{Vr}{2\alpha}\right) \quad (1)$$

where k = conductivity, W/cm-°C
q = heat input, W/cm
r = radius = $\sqrt{x^2 + y^2}$, cm
T = temperature at x, y, °C
T_o = uniform initial temperature, °C
α = thermal diffusivity, cm^2/sec
ϕ = angle radius r makes with x-axis, degrees
K_o = zero-th order modified Bessel function of the second kind.

Temperature gradients and cooling rates may be determined from Eq. (1) by the appropriate differentiation. Letting $\varepsilon = Vr/2\alpha$ and $\gamma = V/2\alpha$ the temperature gradients in the x and y directions, and the cooling rate are, respectively

$$\frac{\partial T}{\partial x} = -\frac{q\gamma}{2\pi k} = e^{-\varepsilon \cos \phi} \left[\cos \phi \, K_1(\varepsilon) + K_o(\varepsilon)\right] \quad (2)$$

$$\frac{\partial T}{\partial y} = -\frac{q\gamma}{2\pi k} \sin \phi \, e^{-\varepsilon \cos \phi} K_1(\varepsilon) \quad (3)$$

$$\frac{\partial T}{\partial t} = -V \frac{\partial T}{\partial x} \quad (4)$$

where K_1 is the first-order modified Bessel function of the second kind.

Equations (1) - (4) can be manipulated so as to yield the heat transfer parameters of interest for correlation with microstructural observations. Cooling rates, temperature gradients, etc., may be calculated with respect to either fixed or moving coordinates using the geometrical relationships shown in Fig. 2b. A discussion of the method of calculation of the important welding parameters follows.

a. Melt Pool Geometry

The shape of the melt pool is defined by the locus of points at which the material temperature is equal to the melt temperature, T_{melt}. This is determined by setting the temperature T in Eq. (1) equal to the melt temperature and solving for the coordinates r and ϕ which satisfy the resulting equation. Because the equation is transcendental it is not possible to solve directly for r as a function of ϕ (or vice versa) and an iterative scheme is required. A numerical algorithm was devised whereby, for a fixed value of ϕ, (with $T = T_{melt}$) Eq. (1) can be solved rapidly for a unique value of r which then determines the melt interface. The x and y coordinates can be obtained from r and ϕ by means of the usual polar coordinate transformation.

b. Maximum Melt Zone Width

The maximum melt zone width can be determined several ways but the simplest method is the following. For a fixed distance y out from the weld centerline the points ahead of the melt isotherm have temperatures lower than those behind it because the melt pool is moving into a region of solid (cooler) material. The temperature gradient is negative at these points, using the coordinate system of Fig. 2b (i.e. it decreases with increasing x). Similarly, temperature decreases behind the melt zone at a fixed distance y and the temperature gradient there is positive. The maximum width of the melt zone (on any isotherm, in general) will therefore be defined by the point where the temeperature gradient with respect to x is zero. Expressing this condition using Eq. (2) yields

$$\cos \phi_{max} \approx - \frac{K_o(\varepsilon_{max})}{K_1(\varepsilon_{max})} \tag{5}$$

where the subscript "max" refers to values at the maximum width. Substituting Eq. (5) into Eq. (1) and rearranging yields

$$\frac{2\pi k}{q} (T_{melt} - T_o) = e^{\varepsilon_{max}} \left|\frac{K_o(\varepsilon_{max})}{K_1(\varepsilon_{max})}\right| \; K_o(\varepsilon_{max}) \tag{6}$$

Equation (6) can be solved iteratively for ε_{max} (it is a single-valued function of ε_{max}) and the radius of the isotherm at maximum width, r_{max}, is given by

$$r_{max} = \frac{2\alpha}{V} \varepsilon_{max} \tag{7}$$

The angle at which r_{max} defines the maximum width of the isotherm is obtained by substituting ε_{max} into Eq. (5). The maximum width of the melt zone, y_{max} is therefore defined by

$$y_{max} = 2 \, r_{max} \sin \phi_{max} \tag{8}$$

c. Heat Transfer Parameters at the Melt Interface

The geometry of the melt interface is shown in Fig. 2a where the unit vector $\vec{n}$ is perpendicular to the tangent of the melt interface at the coordinate (r, ϕ). The temperature gradient and solidification rate along the direction defined by $\vec{n}$ are important because they (along with the cooling rate, $\dot{T}$) determine the characteristics of the recrystallized material in the wake of the melt pool. Resolidification, of course, takes place along the rear boundary of the melt pool from the point of maximum width ($\phi = \phi_{max}$) to the trailing edge of the zone ($\phi = 180°$).

The temperature gradient, G, normal to the melt interface (along the direction $\vec{n}$) is given by

$$G = \sqrt{\left(\frac{\partial T}{\partial x}\right)^2 + \left(\frac{\partial T}{\partial y}\right)^2} \tag{9}$$

where $\partial T/\partial x$ and $\partial T/\partial y$ are given in Eqs. (2) and (3), respectively. The angle that the unit normal, $\vec{n}$, makes with the x-axis χ, is defined as

$$\chi = \tan^{-1}\left(\frac{\frac{\partial T}{\partial y}}{\frac{\partial T}{\partial x}}\right) \tag{10}$$

Since the melt interface moves parallel to the x-axis at a speed V, the component of solidification rate along the normal $\vec{n}$ is

$$R = V \cos x \tag{11}$$

It is clear from Eq. (10) that the solidification rate is a maximum at the trailing edge of the melt pool where $\chi = 0°$ and a minimum at the point of maximum width where $\chi = 90°$.

d. Computer Program for 2-D Deep Welding Model

The equations described above were coded into a FORTRAN computer program on the UTRC Univac 1110. The input parameters include the material properties and welding conditions such as traverse speed and input power. The output of the program comprises the following data.

- The coordinates of the melt pool isotherm in both Cartesian and polar coordinates.

- The calculated value of the maximum width of the melt zone and its location (in polar coordinates) on the melt isotherm.

- The values of cooling rate, temperature gradient, solidification rate, ratio of temperature gradient to solidification rate, and the angle χ which the normal to the isotherm makes with the horizontal - all as functions of position along the rear (solidification) side of the melt pool.

In addition, a computer graphics package was developed to display rapidly computer-generated output such as temperature versus time histories. This capability resulted in substantial manpower savings during the model validation process described below.

2. Validation of 2-D Welding Model

A considerable effort was expended to provide validation of the 2-D heat transfer model. For this case, the analytical predictions of the model were validated by comparisons to two types of experimental measurements. These measurements were as follows:

(1) Comparison of the predicted and measured transient temperature at various locations from the weld centerline.
(2) Comparison of the predicted and measured melt zone width.

To obtain measurements of the transient temperature field in the region of the weld, samples of material (both HY80 and 12-13) were instrumented with thermocouples as shown in Fig. 3a.

Initially, four thermocouple locations were chosen (Stage I) after consideration of the welding parameters: laser power, welding speed, beam diameter, etc. Very fine thermocouples (0.025 cm sheath diameter) were utilized for maximum sensitivity and minimum response time. These were mounted singly in close-tolerance holes drilled to a depth of approximately one-half the sample thickness. Each thermocouple signal was amplified and recorded by a high speed, multi-channel visicorder, with chart speed capabilities of 0.25-203 cm/s. A second, and somewhat complementary, technique of temperature measurement was implemented in order to record the highest cooling rates in the fusion zone. This involved a photomultiplier which was focused on a preselected area 0.25 mm in diameter in order to measure changes in emissivity as a function of time. The output voltage thus generated was recorded by a Nicolet 1090 AR digital

oscilloscope. The acquisition of cooling rate data by this technique proved to be experimentally cumbersome and frequently indecipherable. Consequently, measurement of changes in emissivity as a means to determine cooling rate was abandoned for the remainder of the deep-penetration weld trials.

The cooling rate data obtained by recording the temperature signals from the thermocouples vs time revealed two experimental problems. First, the laser power absorbed by the workpiece was a smaller fraction of the laser power setting than expected, so that the thermocouple positions first selected were too far from the weld fusion zone to give useful readings. Secondly, a comparison of the measured cooling rates with those predicted by the analytical model revealed that the initial sample size was too small. Consequently, the Stage II experimental program employed thermocouple positions which were closer to the fusion zone (Fig. 3b,c), and an increased sample size (Fig. 4). In order to determine the true absorbed laser power, a series of calometric measurements was performed after laser irradiation of a known mass of each alloy. The absorbed power measured in the case of each alloy equaled about 50% of the power in the incident beam. The loss was attributed to reflection plus transmission through the "keyhole" in the fusion zone (Fig. 3a).

A series of four samples each of HY80 and 12-13 were welded with the same welding parameters utilized previously. Temperature measurements from the embedded thermocouples were obtained as a function of both time and distance from the centerline of the fusion zone. The welds were examined metallographically in transverse section in order to determine the dependence of fusion zone width upon power input (Figs. 5 and 6).

Comparisons of the experimentally measured temperature histories and the corresponding analytical predictions were made in the following way. First, the thermocouple readings were taken from the visicorder traces at selected intervals and coded into a computer data file. These values were then converted from millivolts and inches to temperature and time, respectively, using the known thermocouple calibration and the visicorder chart speed. Corrections for thermocouple spacing along the axis of the weld were made knowing the thermocouple spacing and the traverse speed of the laser. The corresponding analytical predictions were made with the heat transfer model using known material properties and the geometry of the thermocouple locations as input. Also input were the laser traverse speed and the absorbed laser power as determined from calorimetric measurements. The analytical predictions were brought to close agreement with the experimental measurements by adjusting the material properties to account for uncertainties in variation with temperature. Once the curves were matched for one of the four test sets for each material the same input data produced nearly identical results for the other three sets, indicating a high degree of reproducibility and accuracy in the experimental tests.

An example of the excellent agreement between theory and measurement is illustrated in Fig. 7 where comparisons are shown for each of the four thermocouples used in one of the tests on HY80. There is seen to be remarkable accuracy in the analytical results, particularly in the prediction of the peak temperatures. The figure also illustrates the utility of the graphics package in that the entire display comprising the figure was created in a matter of seconds. This factor was important because of iterative nature of adjusting the material properties. The distances of the thermocouple locations from the weld centerline were 1.49, 1.69, 1.96, and 2.13 mm for thermocouples #1, 2, 3 and 4, respectively. Figure 8 shows the results for thermocouple #2 on an expanded scale. The welding speed for this run was 50 ipm (2.12 cm/sec) and the absorbed power was 5000 W/cm for the 0.59 cm thick sample.

Similar results were obtained for the alloy 12-13 although the agreement of the measurements with theory was not as exact. A sample of the results for this material is shown in Fig. 9 where the weld speed was 50 ipm and the absorbed power was 7000 w/cm.

For the HY80 the predicted melt zone width was 1.28 mm which was in good agreement with values measured from a cross-section of the weld which varied from 1.67 to 1.01 mm over the near-constant-width section of the weld. For the cross-section shown in Fig. 5, the average width was 1.9 mm, including the enlarged area at the top of the weld. The 12-13 had an average melt width of 2.4 mm and a predicted melt width of 2.0 mm. The agreement is quite reasonable considering the relative nonuniformity of the cross-section due to the "nail head" shape at the top of the weld.

3. Shallow Welding Model

If the shallow welding (skin melting) process is considered to be one-dimensional, the equations of heat conduction are far simpler than for the cases of two or three dimensions, but are still nonlinear because of the latent heat term at the melt interface. This is true even if the properties of the material, such as specific heat and thermal conductivity, are constant. This type of problem is usually solved by numerical solution of the conduction equations or by a finite-element, heat-balance technique (Refs. 4 and 5). In a previous UTRC study of the cooling rates in metals (Ref. 6), a finite-element technique was used to calculate cooling rates based on temperature distributions in the melt layer and solid substrate. The temperature distributions had been previously determined by analog computer solution of the nonlinear (with latent heat) melting problem (Ref. 7). Such methods, while closely approximating the exact solution of the equations, are tedious and time-consuming to set up and usually costly in terms of computer time per case. Hence, an entirely analytical, approximate method for obtaining information on the heat transfer properties at the melt interface was conceived and used to avoid the complexities of a numerical solution and to provide results rapidly and economically.

The surface melting problem then reduces to be one-dimensional, transient heat conduction under the following assumptions.

- The material is a one-dimensional semi-infinite solid (this assumption is valid providing the width of the melted zone is large compared to the melt depth)
- The material is at a constant initial temperature throughout
- Heat is input at the surface of the material and is uniform and constant during the application of power
- Cooling is by conduction only; radiation and convection are neglected lected
  The material is homogeneous with constant properties
- Latent heat is neglected.

Using these assumptions, the heat conduction equation can be solved to yield the following closed-form solution for the transient temperature field during heating and cooling.

During heating:

$$T(x,t) = \frac{q}{k}\left[\sqrt{\frac{4\alpha t}{\pi}}\, e^{-\left(\frac{x}{\sqrt{4\alpha t}}\right)^2} - \operatorname{erfc}\left(\frac{x}{\sqrt{4\alpha t}}\right)\right] + T_o \qquad (12)$$

During cooling:

$$T(x,t) = \frac{q}{k}\left[\sqrt{\frac{4\alpha t}{\pi}}\, e^{-\left(\frac{x}{\sqrt{4\alpha t}}\right)^2} - \sqrt{\frac{4\alpha\gamma}{\pi}}\, e^{-\left(\frac{x}{\sqrt{4\alpha\beta}}\right)^2} - x\left(\operatorname{erfc}\left(\frac{x}{\sqrt{4\alpha t}}\right) - \operatorname{erfc}\left(\frac{x}{\sqrt{4\alpha\beta}}\right)\right)\right] + T_o \qquad (13)$$

where k = conductivity, W/cm-°C
q = heat input, W/cm^2
t = time after start of heat input, sec
T = temperature at depth x, °C
T_o = initial temperature, °C
x = depth beneath the surface, cm
α = thermal diffusivity
$\beta = t - \tau$
τ = dwell time (duration of laser power),
and erfc is the complimentary error function.

For actual welding operations where heat is input over a finite region, the dwell time τ is approximated by dividing the diameter of the laser spot by the welding speed. At the surface of the material (x = 0) Eq. (12) reduces to

$$T(t) = \frac{q}{k}\left(\sqrt{\frac{4\alpha t}{\pi}}\right) + T_o \tag{14}$$

and Eq. (13) becomes

$$T(t) = \frac{q}{k}\left(\sqrt{\frac{4\alpha t}{\pi}} - \sqrt{\frac{4\alpha\beta}{\pi}}\right) + T_o \tag{15}$$

Equations (14) and (15) may be used to quickly calculate the surface temperature of the material at any time during heating or cooling.

During cooling, the transient temperature gradient, G(x,t), and the transient cooling rate, $\dot{T}(x,t)$ may be calculated by direct differentiation. These quantities are given by Eqs. (16) and (17).

$$G(x,t) = \partial T/\partial x = -\frac{q}{k}\left[\operatorname{erfc}\left(\frac{x}{\sqrt{4\alpha t}}\right) - \operatorname{erfc}\left(\frac{x}{\sqrt{4\alpha\beta}}\right)\right] \tag{16}$$

$$\dot{T}(x,t) = \partial T/\partial\, t = \frac{q}{k}\left[\sqrt{\frac{\alpha}{\pi t}}\, e^{-\left(\sqrt{\frac{x}{4\alpha t}}\right)^2} - \sqrt{\frac{\alpha}{\pi\gamma}}\, e^{-\left(\sqrt{\frac{x}{4\alpha\beta}}\right)^2}\right] \tag{17}$$

Finally, the solidification rate, R, is related to G and $\dot{T}$ by the relation

$$\dot{T} = GR \tag{18}$$

where G and R are evaluated at the melt interface.

a. Computer Program for Shallow Welding Model

The system of equations described above was coded into a FORTRAN computer program to quickly evaluate the transient heat transfer conditions that occur during the shallow melting. The heat transfer equations were programmed so as to consider a constant depth of melt using absorbed power density as the primary variable. Of course, the approximate analysis does not include an actual

change of phase; the material is assumed to be "melted" at a given depth of the temperature is above the melting point. The computer algorithm used to calculate the transient heat transfer parameters at the melt interface during solidification is as follows.

For a given depth of melt, d, an absorbed power density, q, is chosen. Since the condition of melting implies a melt temperature, T_{melt}, at depth d, Eq. (12) can be solved iteratively for the time required to produce this condition. Let this time be τ. Thus the material has been surface-heated from time-zero to time-τ with a power density q and melted to a depth d, at which depth the temperature is T_{melt}. The surface temperature, T_{max}, at this time (τ) can be found from Eq. (14). This is the highest temperature that occurs anywhere in the material at any time.

With the material melted to depth d at time τ, the energy input ceases and the material begins to cool. As solidification proceeds, the depth at which the temperature equals T_{melt} moves toward the surface. The surface temperature drops and when it reaches T_{melt} the solidification is complete.* The time at which this occurs, τ', can be determined from Eq. (15). The temperature field in the material during the cooling process (between times τ and τ') is defined by Eq. (13).

To determine the temperature gradient and cooling rate at the melt interface as solidification proceeds toward the surface of the material, it is necessary to establish the position of the interface as a function of time. This can be accomplished by selecting, in the time interval $\tau'-\tau$ (during which solidification occurs), a number of discrete points, and at each point solving Eq. (13) iteratively for the depth at which the temperature equals T_{melt}.

Knowing the depth of the melt interface as a function of time, Eqs. (16) and (17) can be evaluated to yield the temperature gradient G and cooling rate $\dot{T}$ at the interface, and Eq. (18) can then be evaluated for the instantaneous freezing rate R. The ratio G/R at the melt interface can therefore be determined both as a function of time and depth during solidifications.

*Although the mathematics of this analysis do not include actual melting, the above description is still accurate in terms of the temperature history of the melting process.

4. Validation of Shallow Welding Model

A series of shallow-penetration laser welds were made in both 12-13 and HY80 in an attempt to validate the predictions of the shallow-welding heat transfer model. The experiments were conducted for laser output power settings of 3 kW and 5 kW, and welding speeds were varied from 12.7 cm/sec (25 fpm) to 101.6 cm/sec (200 fpm). During the welds the laser was focused to a spot size of about 0.08 cm and the samples were welded at the focal plane. For a spot diameter of 0.08 cm the average incident power density for the 3 kW setting was about 6×10^5 w/cm^2 and about 1×10^6 w/cm^2 for the 5 kW setting.

After the welds were made, the samples were sectioned and examined metallographically to determine the depth of melting. The validation was made by comparing measured and predicted melt depths for the various welding conditions. Because of the physically small dimensions of shallow welds and the very short melting and cooling times involved (on the order of milliseconds), thermocouple measurements of the process were not possible. Model validation was therefore restricted to an examination of the weld cross sections.

Enlarged (200X) cross sections of shallow penetration welds in 12-13 are shown in Fig. 10 for a power setting of 3 kW. The reduction in depth of penetration is evident as welding speed is increased from 50 fpm to 150 fpm. Figures 11 and 12 show cross sections in the same material for a 5 kW power setting and welding speeds varying from 25 fpm to 200 fpm. Table I summarizes the results from the shallow weld measurements for 12-13 and HY80. The values shown for 12-13 correspond to the cross sections shown in Figs. 10, 11 and 12. The depth and width shown are the maximum cross-sectional values and the dwell time is the time the laser remains on a location and is obtained by dividing the spot size of 0.08 cm by the welding speed. The dwell time corresponds to the time τ used in Eqs. (12) through (17).

Figure 13 shows the melt depth measurements of Table I for 12-13 superimposed on the predicted depth-versus-weld speed predictions of the shallow weld heat transfer model. The dashed lines show the predicted depth-speed variations for absorbed power densities of 50, 75, and 100 kW. Very good agreement between predicted and measured results is shown for the 5 kW power setting while the 3 kW trend does not agree as well. The actual absorbed power density for the 5 kW setting would appear to be about 65 kW/cm^2 which would indicate that about 6.5% of the incident power was absorbed. This calculation is based on an incident flux of 1×10^6 W/cm^2 assuming a spot size of 0.08 cm.

The variation of melt depth with absorbed power as predicted by the model agrees reasonably well with the measured data. As calculated above, the UTRC 12-13 absorbs about 6.5% of the incident flux at 5 kW corresponding to about 65 kW/cm^2. Assuming the percent of absorbed power stays constant, the 3 kW power setting should result in about 39 kW/cm^2 of power being absorbed (with 6×10^5 W/cm^2 incident). This value is close to the 50 kW line predicted by the model.

The double abscissa of Fig. 13 also shows the dwell time τ corresponding to the weld speed and the estimated spot size of 0.08 cm. It should be noted that the depths recorded in Table I are maximum values and there is also some uncertainty in the diameter of focused laser beam so that an exact estimate of the absorbed power fraction is difficult to make.

Another factor leading to disparity between predicted and measured results is the fact that the shallow-weld cross sections were not of completely uniform depth. The width-to-depth ratios, however, were reasonably large, being in the range of 4 to 10. Uncertainty in the intensity profile of the beam at the workpiece makes it difficult to specify an exact spot size, but the intensity profile was surely not uniform. A more uniform melt depth might have been obtained if the workpiece was moved away from the exact focal plane location thereby making the intensity profile less peaked. The value of 0.08 cm for an "effective" spot size appears to be validated by the measured melt widths shown in Table I. The values are seen to be less than 0.08 cm except for the slowest weld speeds. This effect would follow considering the lateral conduction of heat which must take place on the sides of the melt zone. Melt width can be seen, from Table I, to decrease uniformly with increasing weld speed.

Figure 14 shows the predicted and measured depth-versus-weld speed variations for HY80. The depths predicted for the 5 kW power setting are in reasonable agreement with those for an absorbed power density of 75 kW/cm^2. This indicates about 7.5% of the indicated power was absorbed for the 5 kW setting. Results for the 3 kW setting show reasonable agreement with the predicted trends for variations with both weld speed and incident power. Assuming that the 7.5% absorption factor remains constant, the absorbed flux for the 3 kW power setting would be about 45 kW/cm^2. This value is close to the 50 kW/cm^2 line predicted by the model. As in Fig. 13, the laser dwell time is shown along with weld speed as the independent variable.

In general, the prediction by the 1-D heat transfer model of melt depth as a function of weld speed and absorbed power is in good agreement with measured values, considering the uncertainties and nonuniformity of the incident beam.

It is interesting to note that the curves of melt depth as a function of weld speed trend towards intersecting the weld speed axis at a melt depth of zero, rather than extending out asymptotically. In fact, there is a minimum dwell time, τ_{min}, for which the surface temperature cannot be raised above the melt temperature for a given incident flux. This value can be obtained by solving Eq. (14) for $t = \tau_{min}$ when $T = T_{melt}$. The result is

$$\tau_{min} = \frac{\pi}{4\alpha}\left[\frac{k(T_{melt}-T_o)}{q}\right]^2 \qquad (19)$$

The corresponding maximum weld speed is

$$V_{max} = \frac{d}{\tau_{min}} \tag{20}$$

where d = the effective spot diameter.

The minimum weld speed for HY80 at an absorbed flux of 45 kW/cm^2 is calculated from Eq. (19) to be about 70 cm/sec which corresponds to a dwell time of about 0.001 sec (Eq. 20). These results are in good agreement with the intersection of the 5 kW (45 kW/cm^2) line with the zero-melt-depth line of Fig. 14.

TASK III - MATERIALS ANALYSIS

It was originally proposed to conduct directed energy welding experiments using a high power density electron beam gun constructed within the chamber of an Auger electron spectrometer to study segregation of impurities to crack surfaces. Unfortunately, it became evident that the equipment necessary for these types of experiment would not be sufficiently developed during the performance period of this program. Consequently, the emphasis of the program was directed towards the extremely important question of the relation between microstructure and cracking behavior in laser welded alloys. Furthermore, although it was suggested that studies be carried out on both an alloy system of the Ni-base variety and HY80 steel, it has only been possible, in the time given, to perform thorough studies on one alloy system. The system chosen for study was the Ni-Al-Mo ternary, the reasons for our choice being given below. It should be pointed out that detailed microstructural analysis of rapidly solidified structures is very time consuming, and this fact has been a primary cause for us examining only one alloy system during the performance period. It has been proposed that the response of HY80 steel to laser welding be studied in some detail during the second year of work on this program.

A. Cracking of Laser-Welded Ni-Al-Mo Alloys

Many advanced Ni-base superalloys for gas turbine engine applications have been based on the Ni-Al-Mo alloy system, since the derivative alloys have shown remarkable increases in creep strength and other properties compared to those alloys currently in service. It seemed useful, then, to study in some detail the response of this alloy system to laser welding, and, in particular, to investigate whether a relationship between microstructure and weld-cracking exists. An added advantage of this choice of alloy system stems from the fact that its laser-welding response had already been established during the DARPA-sponsored ONR-monitored program involving the fabrication of a scale-model turbine disk using the LAYERGLAZE™ process. In this way, it was possible to effect significant exonomies in laser time devoted to the materials analysis task, and slso to permit a useful scientific interaction between two DoD-sponsored programs to take place.

The cracking responses of three different alloys to partial penetration laser welding are given in Table II. These three alloys, Ni-12Al-11Mo, Ni-12Al-13Mo and Ni-12Al-15Mo (termed 12-11, 12-13 and 12-15, respectively where the concentrations are given in atomic %), do in fact provide a unique set of materials with which to make a study of the effect of microstructure on weld cracking. Thus, it can be seen that only very small concentration changes, viz. the substitution of 2 at. % Mo for Ni in each case, cause the cracking behavior to change from substantial to essentially none and then to moderate cracking. This is a remarkable effect of elemental concentration, and its occurrence is an additional reason for the choice of this alloy system for study.

One may summarize the results of the experiments and alloy data listed in Table II as follows:

1. Small changes in Mo content causes cracking behavior to alter substantially.

2. The as-welded microhardness increases with Mo content, there being and especially large increase between alloys 12-13 and 12-15.

3. The freezing range first increases relatively markedly with Mo content, and then decreases slightly. It should be pointed out that differential thermal analysis (DTA) measurements are not particularly sensitive to the accurate determination of the last liquid to freeze, so that the solidus temperatures may, in fact, be somewhat in error. However, they do permit an estimate of the freezing range to be established.

4. The γ' solvus temperature increases with Mo content.

5. The DO_{22}-Ni_3Mo solvus temperature decreases with Mo content, although no evidence for significant precipitation has been found in the alloy 12-11.

These interesting observations do not either singly or in combination permit an explanation for the cracking behavior to be developed. Thus, since the microhardness of the as-welded alloys increases with Mo content, it is difficult to propose that the difference in strengths of the alloys is necessarily relevant to cracking. Similar difficulties also exist if explanations involving the freezing range or γ' solvus temperature are put forward. Furthermore, one may positively assert that since DO_{22}-Ni_3Mo is essentially absent from alloy 12-11, that the occurrence of this phase transformation plays no role in the cracking mechanism. Because the profound effect of minor changes of Mo content could not be explained on the basis of the parameters described above, experiments were performed to investigate whether a relationship between microstructure and laser-weld cracking exists.

B. Microstructural Observations

It was felt important to study both the as-chill cast and laser welded microstructures of each of the three alloys. In this way, it should be possible to determine the effects of rapid solidification associated with laser processing on microstructural modifications. However, the difficulty in preparing useful thin foils from laser treated material and the relatively high dislocation density of such alloys make meaningful TEM/STEM analysis very difficult. To overcome this problem, rapidly solidified specimens were prepared in an iced-brine quenching rig, where solidification rates were estimated to be in a range similar to those associated with laser processing. The experiment consisted simply

of passing an electric current through a thin strip of the given alloy until melting begins at which point the assembly is spontaneously dropped into the iced-brine quenching medium. Provision was made for performing this experiment in an inert atmosphere. In this way, specimens were produced whose thermal histories were analogous to those characteristic of laser processing. While the phase constitution and distribution will fairly accurately resemble that existing in the laser treated specimens, it should be noted that the dislocation microstructure will be very different in the two rapidly solidified materials. In summary, two tupes of microstructure were studied, namely as-chill cast and iced-brine quenched.

1. As-Chill Cast Microstructures

Alloy 12-11. The microstructure, depicted in Fig. 15, consists of a distribution of γ and γ', with essentially no DO_{22}-Ni_3Mo precipitation. The grain boundaries appeared to be relatively "clean".

Alloy 12-13. Within the grains, the microstructure was similar to that of 12-11, except that some DO_{22}-Ni_3Mo had precipitated in the matrix γ. However, significant grain boundary precipitation occurred, (See Fig. 16) consisting of γ' and δ(NiMo). The γ' appeared to be relatively continuous along the boundary.

Alloy 12-15. Again, within the grains, the microstructure was similar to that in the two cases described above, except that there seemed to be some evidence suggesting increased formation of DO_{22}-Ni_3Mo. Grain boundary precipitation had again occurred, but in this case, the γ' was "blocky" in nature. In addition to the γ', α-Mo was also present at the grain boundaries (Fig. 16), and this indicates that the addition of 2 at. % Mo to 12-13 results in a composition lying in a different phase field. Presumably, the precipitation behavior is sufficiently different so that "blocky" γ' forms instead of a continuous film. In all three microstructures, the volume fraction of γ' in the matrix appeared to be fairly similar.

2. Iced-Brine Quenched Microstructures

The effect of rapid solidification on these three alloys was primarily to reduce the size of the γ' within the grains from approximately 0.1μm in the as-chill cast material to ~20-100Å in the quenched specimens, see Fig. 17. However, while the grain boundaries for 12-11 remain "clean", grain boundary precipitation for the two alloys 12-13 and 12-15 remained essentially the same as that described above for the as-chill cast microstructures. Figure 18 shows the structure of a grain boundary in quenched 12-13.

In summary, the major difference between the various microstructures lies in the precipitation at the grain boundaries. We feel that a particularly significant observation is the morphology of the grain boundary γ'. Thus, in 12-11, the grain boundaries are "clean"; in 12-13, γ' and δ(NiMo) are present, and the γ' is in the form of long (almost) continuous layers on either side of the boundary; and finally, in 12-15, γ' and α-Mo are the main constituents, but in this case the γ' is in "blocky" form. These morphologies of γ' at the grain boundaries cause an analogy to be drawn with the role of Hf in improving ductility in MAR M200 (Ref. 8). Thus, doping MAR M200 with Hf produces large scale precipitation of γ' at such boundaries, usually in blocky form, but where the ideal morphology involves the formation of grain boundary layers of γ'. There are several proposed mechanisms for increased ductility caused by such morphology and precipitation, but one that is commonly accepted involves slip dispersal by the γ' at such boundaries (Refs. 8,9). Thus, we tentatively propose that the effect of Mo content on cracking behavior is due to the precipitation and morphology of γ' at the grain boundaries of the as-chill cast and subsequently laser-processed material. On this basis, alloy 12-13 would be expected to exhibit the largest degree of cracking resistance, as is shown in Table II.

Since our model is microstructure dependent, it was important to test our assumption by modifying the microstructure of the most crack resistant alloy (12-13) and show that without a layer of γ' at the grain boundaries, the alloy becomes susceptible to cracking. The most convenient method of achieving this was to homogenize the as-chill cast structure. This was done, and the microstructure exhibited γ/γ' dispersions within the grains (together with a small amount of DO_{22}-Ni_3Mo formation within the matrix), but little or no grain boundary precipitation (Fig. 19). A further check was made by quenching such homogenized material, and in common with all quenched structures an extremely fine dispersion of γ' in γ was produced, but the grain boundaries were more or less "clean". Thus, the grain boundary morphology and structure of alloy 12-13 had been drastically altered through heat treatment. Laser welding of this homogenized alloy did, indeed, produce cracking, in agreement with the model described above. Further work is required to unequivocally establish the validity of our model, but the cracking of the homogenized material does lend strong support to the notion that the morphology and structure of grain boundaries is very important. Particularly significant is the observation that it is the initial structure of the material to be welded that plays a leading role in predicting cracking behavior. Since the dwell-time in the liquid state is relatively short in laser processing, there is little chance for homogenization to occur during welding. Thus, large scale inhomogeneities will be expected to persist through the welding process. Moreover, the fact that grain boundary morphology appears to be significant, implies that the cracking is occurring in the solid state rather than during freezing.

It may be asserted that the cracking behavior resulting from variations in Mo content may be attributed to changes in chemistries of the γ/γ' phases causing corresponding modification in properties (e.g. mechanical strength). Therefore, attempts were made during this study to determine phase chemistries using STEM. However, it was not possible to determine these quantities absolutely because of the occurrence of surface layers on electropolished samples (thinned for STEM purposes) (Ref. 10). The results of the STEM analysis when considering relative changes in phase chemistries do not in any way lead to a conclusion concerning the role of this parameter in weld cracking. Studies are presently in progress that are aimed at devising methods to remove these surface layers, and once this is possible, the STEM analysis will be repeated.

An interesting observation in the quenched samples leads again to the conclusion that the grain boundary morphology and structure play a dominant role in weld cracking. In all quenched samples studied, the dislocations in the matrix resemble those normally observed in a single phase material, (see Fig. 17). This is to be expected since the γ' distribution is present on such a fine scale. The dislocations are, therefore, essentially unaffected by the presence of γ' within the matrix. It is the deformation process at the grain boundary that appears to be somewhat more significant.

REFERENCES

1. D. T. Swift-Hook and A. E. F. Gick: Penetration Welding with Lasers, Welding Research Supplement, November 1973, pp 492-s - 499-s.

2. D. Rosenthal: The Theory of Moving Sources of Heat and Its Applications to Metal Treatments, Transactions of the ASME, November 1946, pp 849-866.

3. P. S. Meyers, O. S. Uyehara and G. L. Borman: Fundamentals of Heat Flow in Welding, Welding Research Council Bulletin No. 123, July 1967, pp 1-46.

4. W. D. Murray and F. Landis: Numerical and Machine Solutions of Transient Heat-Conduction Problems Involving Melting or Freezing. Transactions of the ASME, pp 106-112, May 1959.

5. R. C. Ruhl: Cooling Rates in Splat Cooling. Mater. Sci. Eng., 1, pp 313-320, 1976.

6. L. E. Greenwald: Calculations of Freezing Rates in Metals. United Technologies Research Center Report R75-111321-1, October 1975.

7. M. I. Cohen: Melting of a Half-Space Subjected to a Constant Heat Input. Journal of the Franklin Institute, Vol. 283, #4, pp 271-285, April 1967.

8. J. E. Doherty, B. H. Kear and A. F. Giamei, 1971, J. Metals, pp 59-62.

9. B. H. Kear, private communication.

10. H. L. Fraser and G. P. McCarthy, 1981, in preparation.

Table I

SUMMARY OF SHALLOW WELD MEASUREMENTS

UTRC 12-13

Laser Power (kW)	Welding Speed (cm/sec)	Dwell Time (sec)	Depth (cm)	Width (cm)
3	25.4	.00315	.008	.0460
3	50.8	.00157	.00575	.0435
3	76.2	.00105	.005	.0335
5	12.7	.00630	.020	.0876
5	25.4	.00315	.015	.0730
5	50.8	.00157	.0088	.050
5	76.2	.00105	.006	.0440
5	101.6	.000787	.004	.0325

HY80

Laser Power (kW)	Welding Speed (cm/sec)	Dwell Time (sec)	Depth (cm)	Width (cm)
3	25.4	.00315	.006	.0425
3	50.8	.00157	.0063	.0355
3	76.2	.00105	.0028	.0225
5	12.7	.00630	.0155	.0826
5	25.4	.00315	.009	.0826
5	50.8	.00157	.0085	.0700
5	76.2	.00105	.0055	.0505
5	101.6	.000786	.00380	.0243

Table II

Weld-Cracking Response and Alloy Data for Given Alloys

Alloy	Cracking Behavior None	Moderate	Substantial	As-welded Microhardness VHN, 200 gm	Liquidus °C	Solidus °C	γ' Solvus	Ni_3Mo Solvus
Ni-12Al-11Mo			X	433	1386	1363	1173	
Ni-12Al-13Mo	X			492	1377	1297	1195	913
Ni-12Al-15Mo		X		591	1365	1289	1200	907

DEEP-PENETRATION WELD MODEL

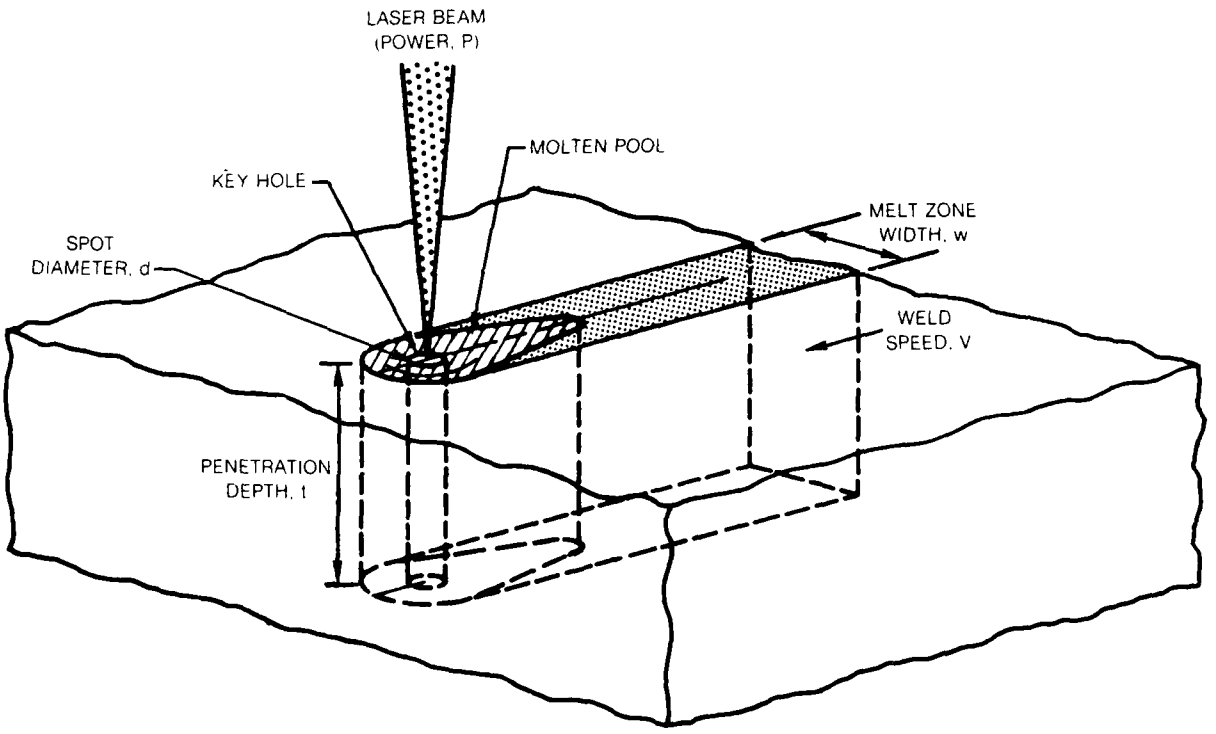

80-10-104-2

FIG. 2

SCHEMATIC REPRESENTATIONS OF TEMPERATURE FIELD MODEL

a) TEMPERATURE FIELD GEOMETRY

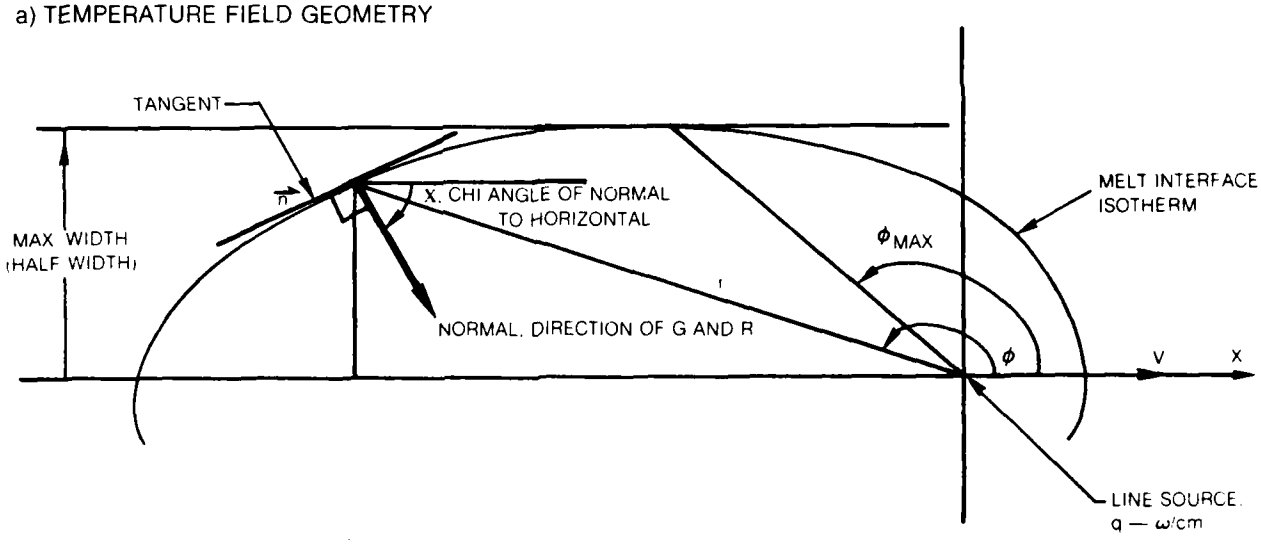

b) COORDINATE SYSTEM

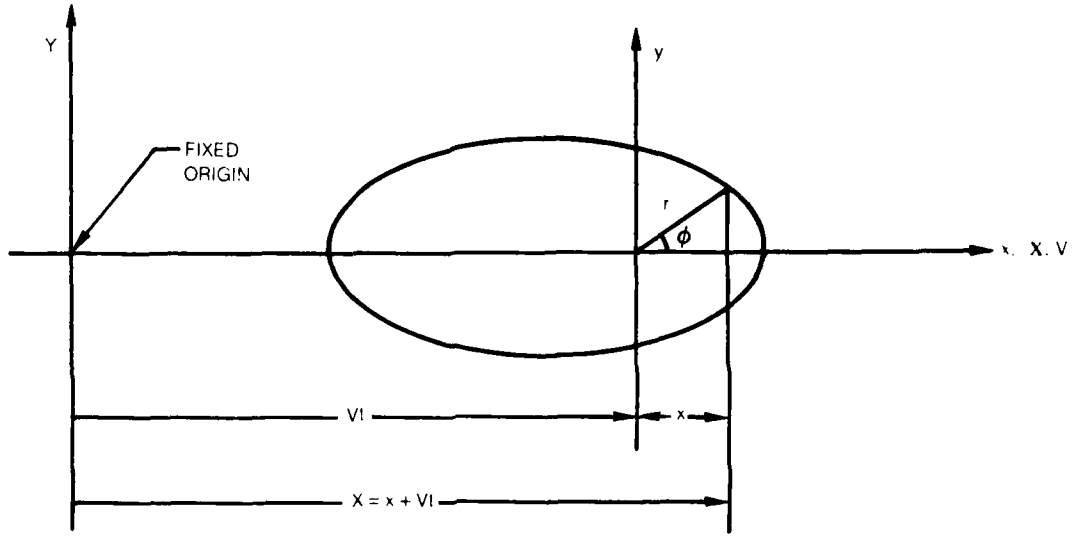

80-10-104-1

THERMOCOUPLE LOCATIONS — DEEP PENETRATION WELD

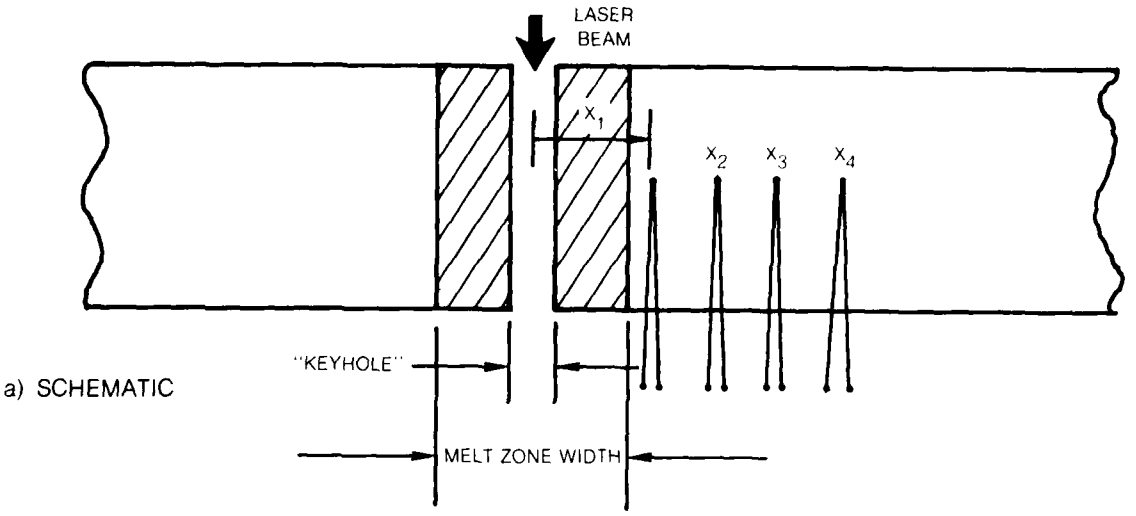

a) SCHEMATIC

b) ALLOY 12-13

STAGE I LEFT SIDE OF WELD SEAM
STAGE II RIGHT SIDE OF WELD SEAM

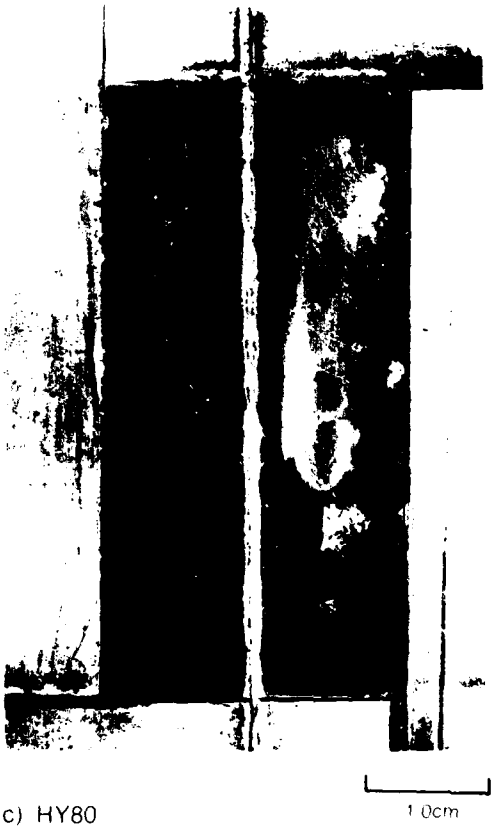

c) HY80

STAGE I LEFT SIDE OF WELD SEAM
STAGE II RIGHT SIDE OF WELD SEAM

ENLARGED SAMPLES FOR STAGE II EXPERIMENTS

a) HY80

5cm

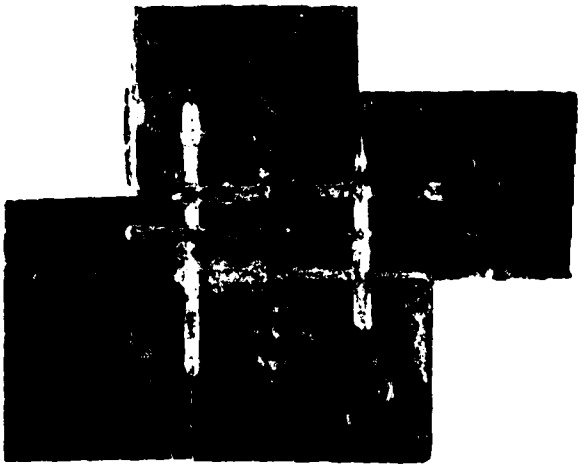

b) ALLOY 12-13

5cm

HY80: TYPICAL WELD CROSS SECTION

AVERAGE MELT WIDTH = 5 mm

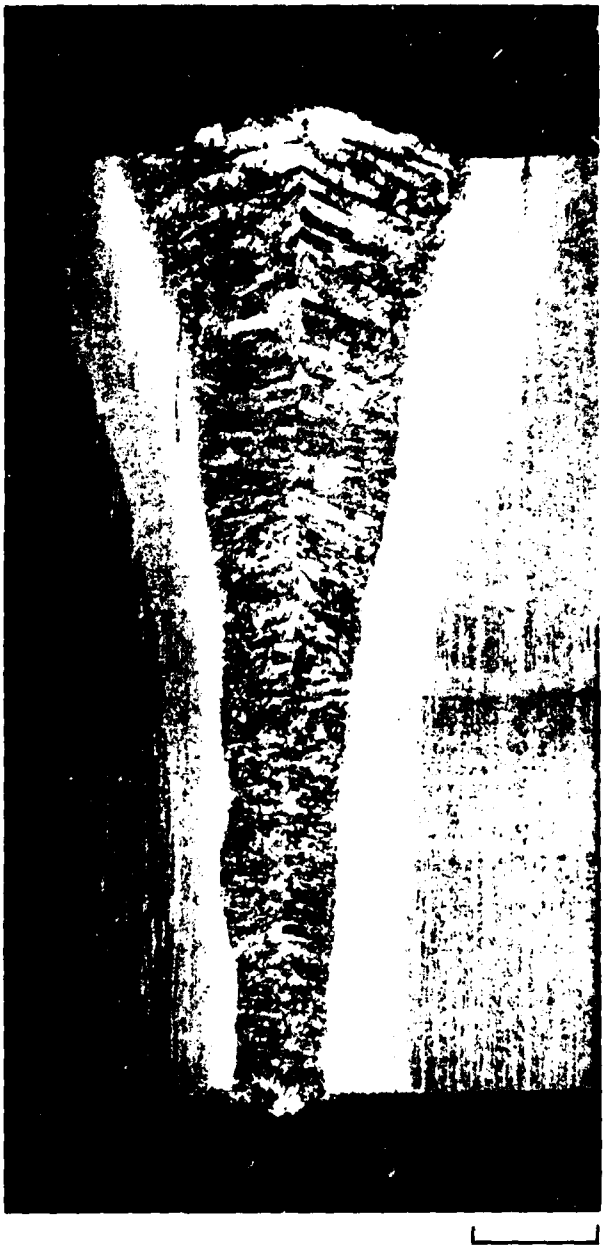

UTRC 12-13: TYPICAL WELD CROSS SECTION

AVERAGE MELT WIDTH = 2.4mm

FIG. 7

COMPARISON OF TEMPERATURE HISTORIES

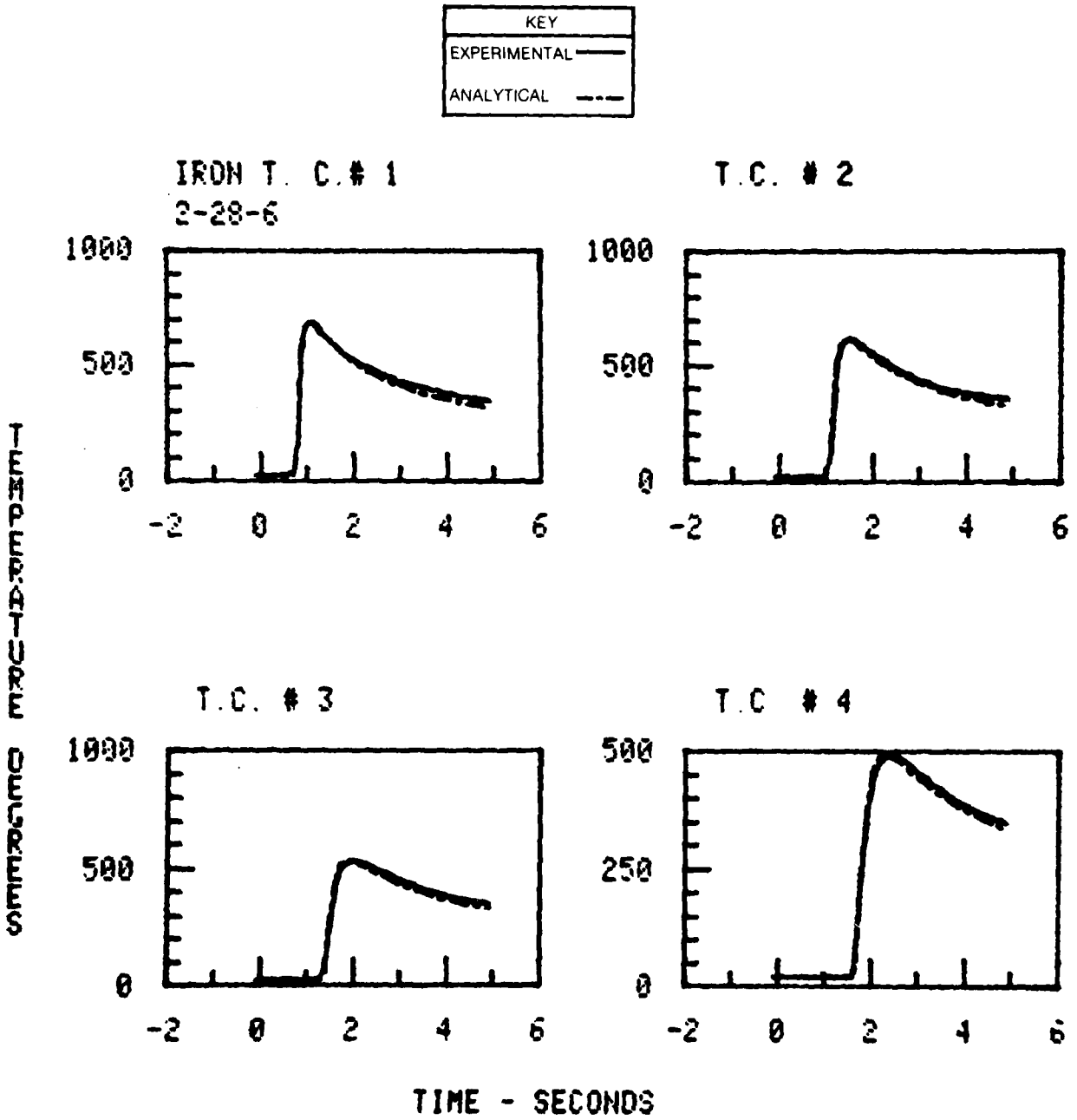

80-4-52-1

COMPARISON OF TEMPERATURE HISTORIES

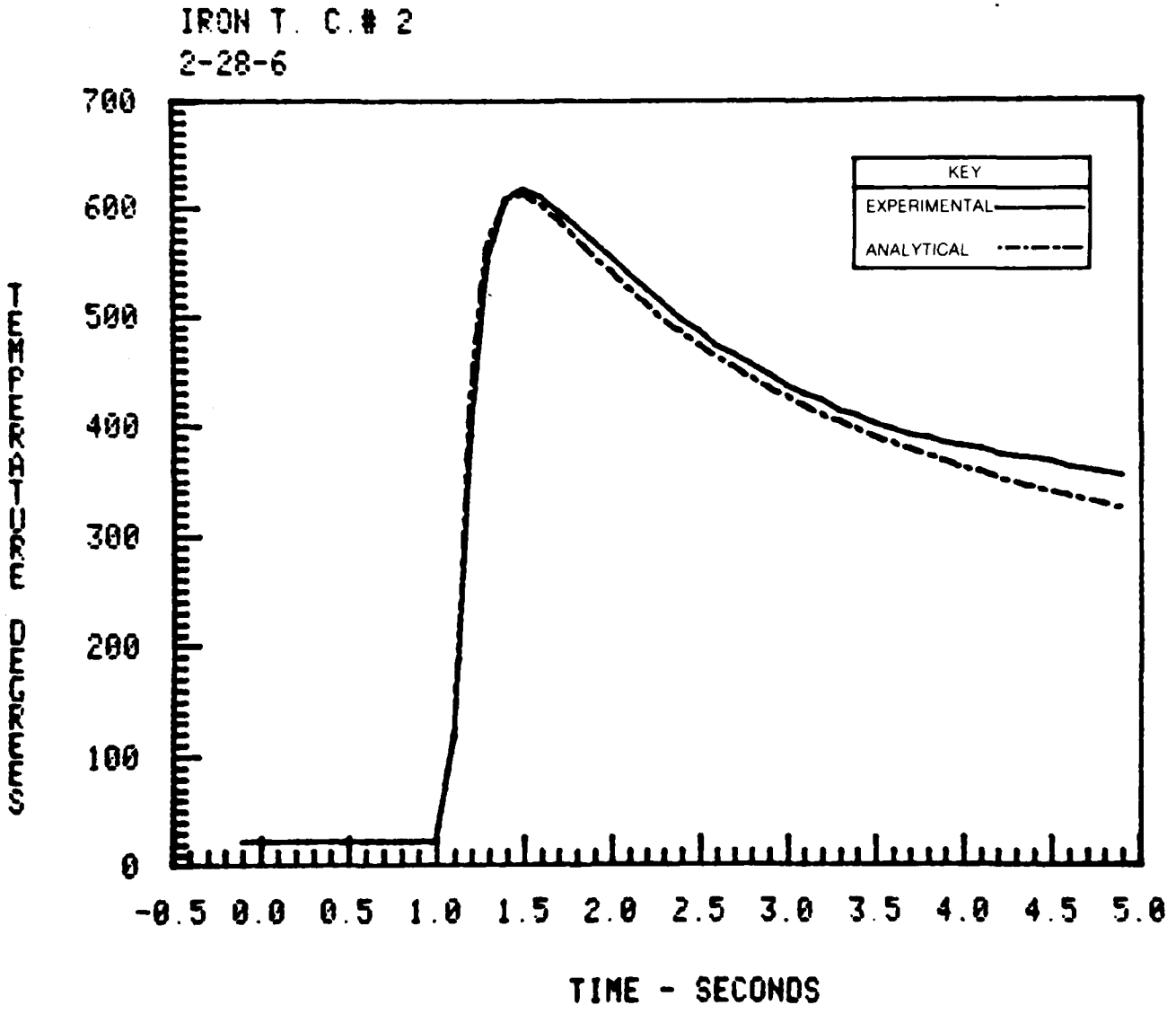

80-4-52-2

COMPARISON OF TEMPERATURE HISTORIES

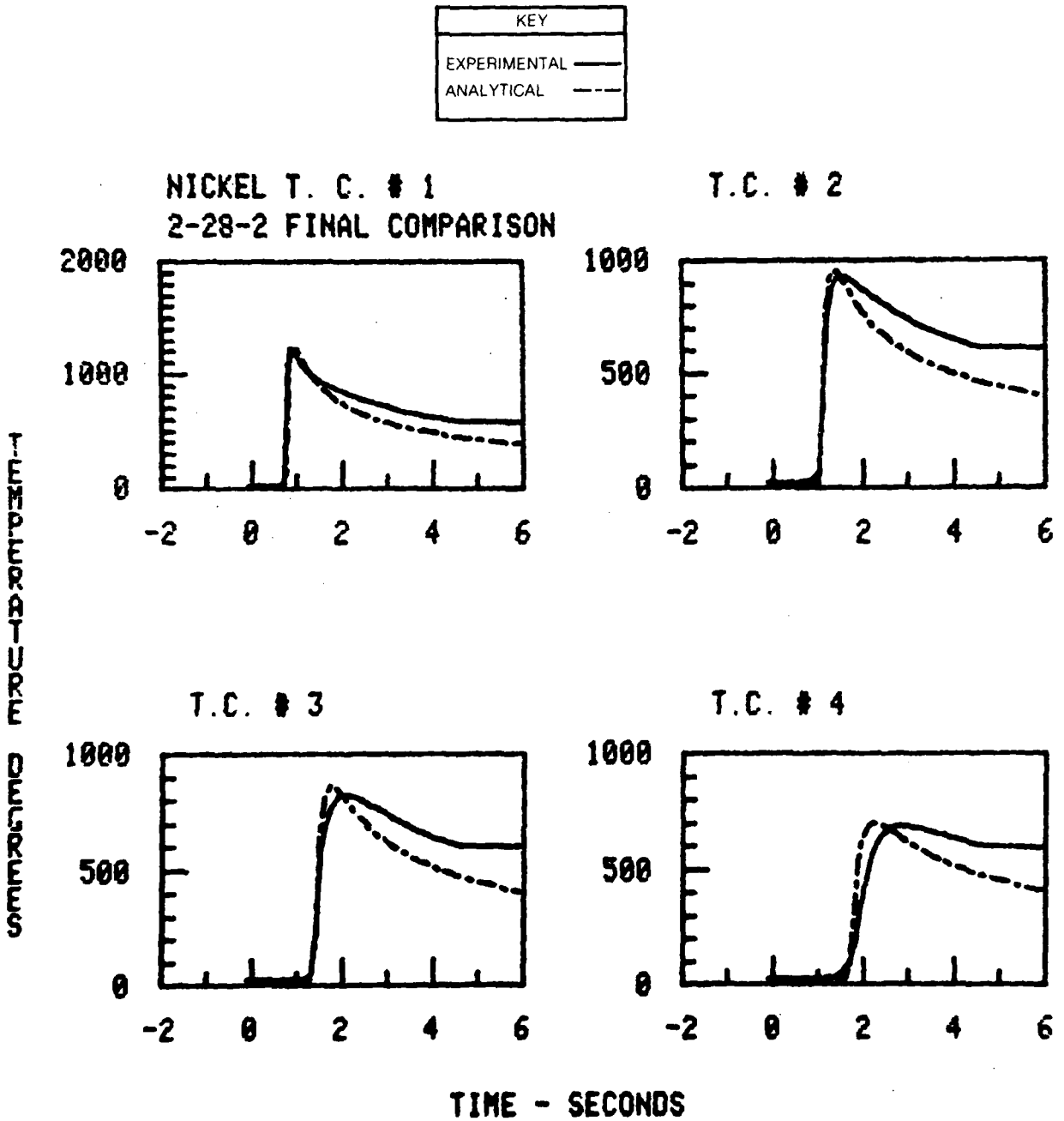

80-10-104-6

SHALLOW PENETRATION WELDING 12-13 NICKEL ALLOY

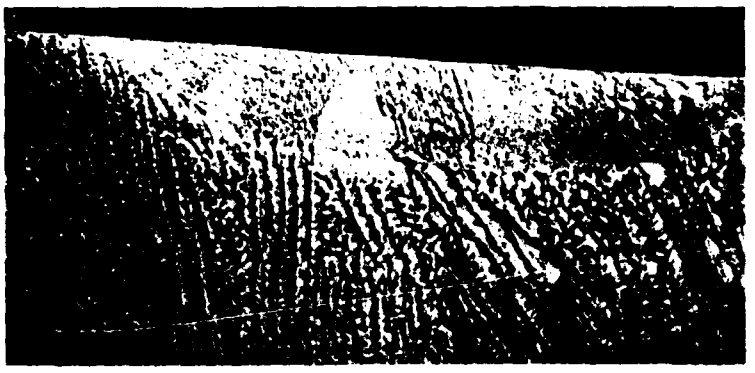

a) 3kW, 50 fpm (25.4 cm/sec)

b) 3kW, 100 fpm (50.8 cm/sec)

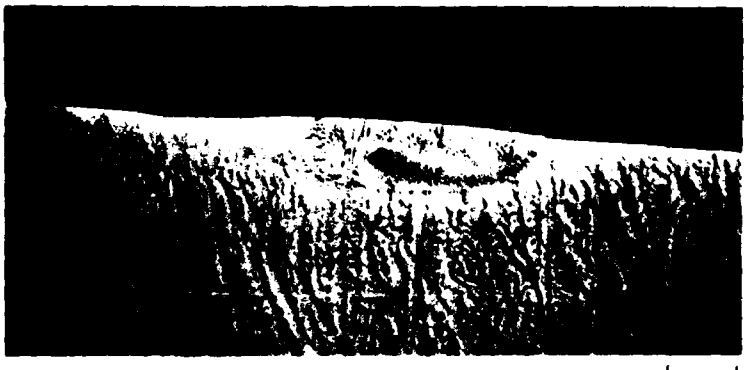

c) 3kW, 150 fpm (76.2 cm/sec)

SHALLOW PENETRATION WELDING 12-13 NICKEL ALLOY

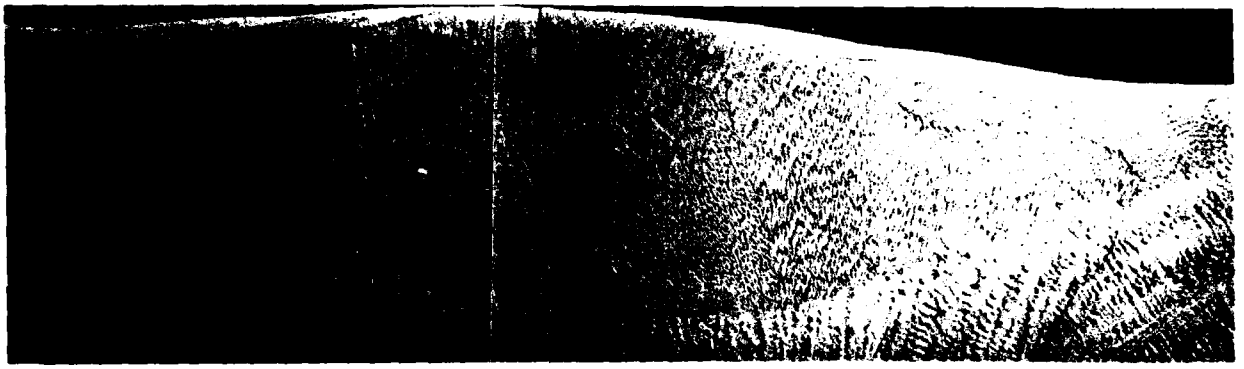

a) 5kW, 25 fpm (12.7 cm/sec)

50 μm

b) 5kW, 50 fpm (25.4 cm/sec)

50 μm

80-10-104-5

FIG. 12

SHALLOW PENETRATION WELDING 12-13 NICKEL ALLOY

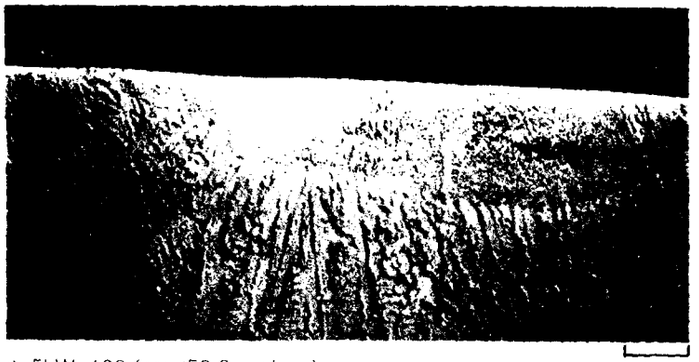

a) 5kW, 100 fpm (50.8 cm/sec)

b) 5kW, 150 fpm (76.2 cm/sec)

c) 5kW, 200 fpm (101.6 cm/sec)

80-10-104-3

FIG. 13

MELT DEPTH VS. WELD SPEED AND DWELL TIME

MATERIAL: UTRC 12-13

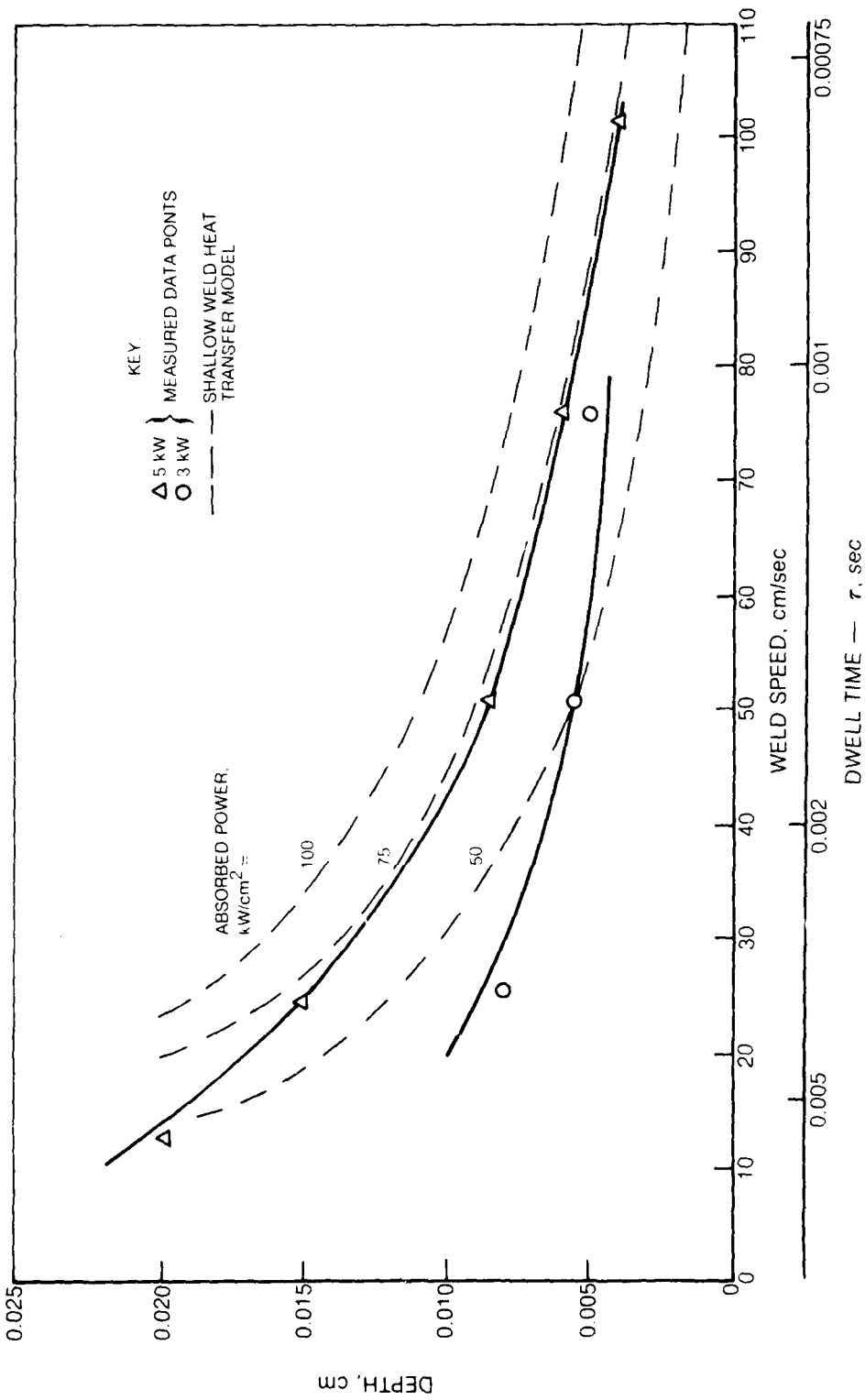

80-10-104-10

FIG. 14

MELT DEPTH VS. WELD SPEED AND DWELL TIME

MATERIAL: HY80

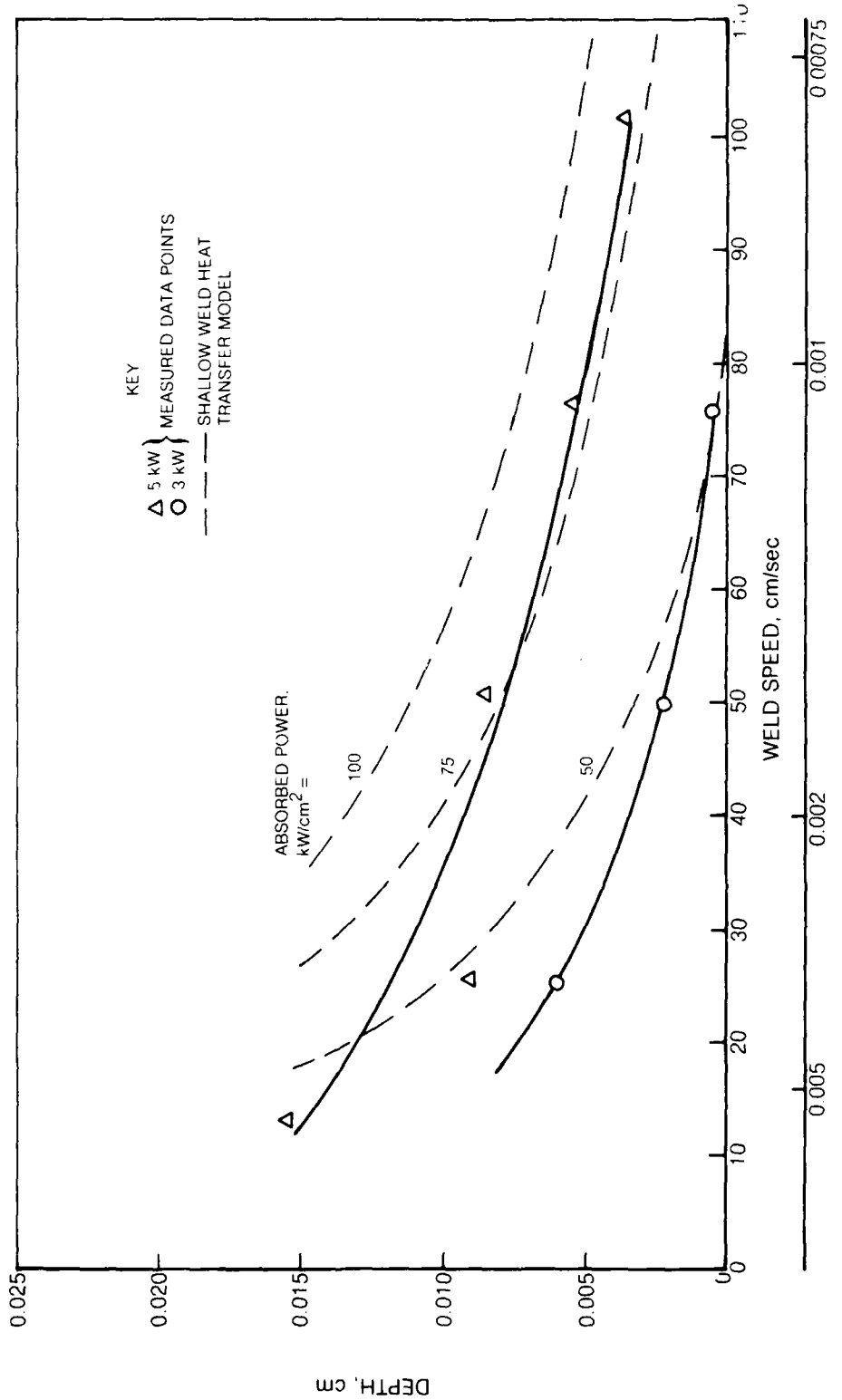

80-10-104-9

AS-CHILL CAST STRUCTURE OF ALLOY 12-11, SHOWING A GRAIN BOUNDARY WITH NEGLIGIBLE SECOND PHASE PRECIPITATION

TRANSMISSION ELECTRON MICROGRAPH 120kV ACCELERATIVE VOLTAGE

AS-CHILL CAST STRUCTURE OF ALLOY 12-13, SHOWING GRAIN BOUNDARIES AND ASSOCIATED PHASE CONSTITUTION

TRANSMISSION ELECTRON MICROGRAPHS. 120kV ACCELERATING VOLTAGE

FIG. 16b

AS-CHILL CAST STRUCTURE OF ALLOY 12-15, SHOWING GRAIN BOUNDARIES AND ASSOCIATED PHASE CONSTITUTION

TRANSMISSION ELECTRON MICROGRAPHS 120kV ACCELERATING VOLTAGE

80-11-103-3

MICROSTRUCTURE OF ALLOY 12-13 FOLLOWING CHILL CASTING AND ICED-BRINE QUENCHING FROM THE MELT

TRANSMISSION ELECTRON MICROGRAPH 120 kV ACCELERATING VOLTAGE

MICROSTRUCTURE OF GRAIN BOUNDARY IN ALLOY 12-13 FOLLOWING CHILL CASTING AND ICED-BRINE QUENCHING FROM THE MELT

TRANSMISSION ELECTRON MICROGRAPH. 120kV ACCELERATING VOLTAGE

80-11-103-5

MICROSTRUCTURE OF GRAIN BOUNDARY IN ALLOY 12-13 IN A SOLUTION-TREATED SAMPLE

THERE IS LITTLE OR NO SIGNIFICANT PRECIPITATION ASSOCIATED WITH THE BOUNDARY

TRANSMISSION ELECTRON MICROGRAPH 120kV ACCELERATING VOLTAGE

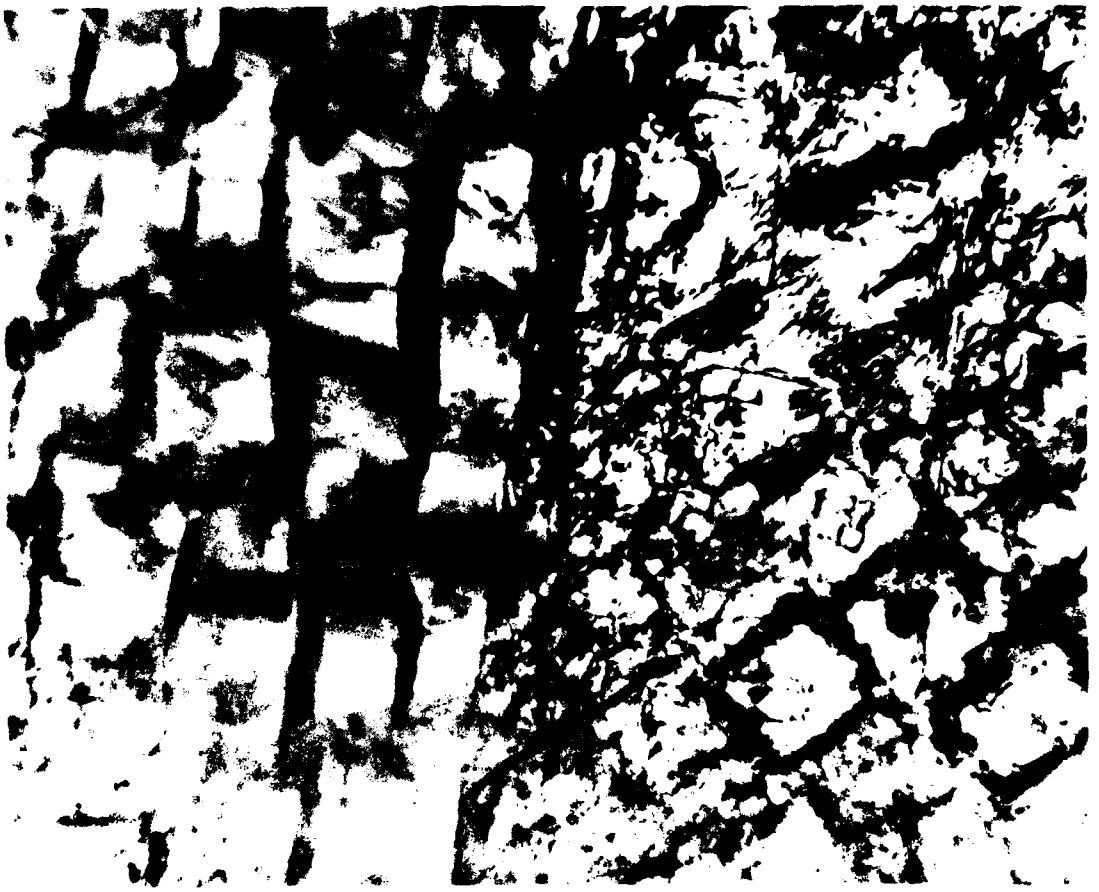

80-11-103-6